ROYAL SOCIETY
OF CHEMISTRY

PAPER

Check for updates

A hydrophobic–superoleophilic 2D Zr-based alkyne-rich metal–organic framework for oil/water separation and solar-assisted oil evaporation†

Qian-Ru Luo,‡ Yuan-Hui Zhong, [ID] ‡ Lai-Hon Chung, [ID] * Zhixin Jiang, Qia-Chun Lin, Xin-Ke Xu, Xinhe Ye, Wei-Ming Liao [ID] and Jun He [ID] *

A 2D layered Zr-based metal–organic framework (MOF), Zr**L1**, was assembled from Zr(IV) ions and backfolded alkyne-rich dicarboxylate linker (**L1**$^{2-}$). Structurally robust and chemically stable Zr**L1** was dip-coated on polyurethane (PU) to give a composite Zr**L1**@PU, which exhibited significantly enhanced oil/water separation performance (maximum absorption capacity: 66.19 g g^{-1}, separation efficiency: 99.3%, selectivity: water totally excluded, and permeability: 5340 L m^{-2} h^{-1}) when compared with pristine PU. More importantly, Zr**L1**@PU maintained steady performance and framework stability even upon 20 cycles of operation. Given that Zr**L1**@PU is photothermally active, it was taken for solar-driven evaporation of the oil harvested during oil/water separation, and the evaporation efficiency of Zr**L1**@PU (complete evaporation within 25–40 minutes) outperforms that of pristine PU (30 wt% of the selected oil still remained within the same illumination period). This study represents an illustrative example giving insights into the rational design of hydrophobic/superoleophilic framework for fabricating efficient durable self-cleaning oil/water separator.

Introduction

Oil-contaminated water from industrial effluent and oil spillage incidents degrades drinkable water and threatens marine lives.[1,2] Nowadays, various industrial approaches, such as air flotation, centrifugation, coagulation, and gravity-driven separation, have been developed to implement oil separation from water. However, these methods are complicated to process and costly, making them inefficient to address oil/water separation. Alternatively, porous adsorbents, including cotton, linens, and zeolites, have been applied to oil/water separation; however, their low adsorption capacity, poor recyclability, and secondary pollution generation limit their further application in oil/water separation.[3,4] As a result, various modified porous materials emerged as new platforms for exploring competent oil/water separator, and this research area continues unabated.[5–14] Considering oil adsorbents, materials with 'special wettability', referring to wetting properties with liquid contact angles above 150° or smaller than 10°, represent a novel class of aqueous-

phase oil adsorbent because of their easy operation.[15] It is well-established that superhydrophobic materials exhibit water contact angle >150° while superoleophilic materials give oil contact angle <10°.[15] Specifically, hydrophobic-oleophilic adsorbents are favourable for highly selective oil/water separation by extracting oils from the water body (hydrophobic: repel water and leave it behind; oleophilic: take up oil actively).

Metal–organic frameworks (MOFs), constructed from regular coordination between metal clusters/ions and multitopic organic linkers, represent a class of crystalline polymer suitable for the design of special wettability gifted materials owing to their well-defined network, rich linker functionalities, and diversified yet predictable topologies.[16–28] To obtain hydrophobic MOFs, there are some common strategies: (1) the fluorination/alkylation of MOF either through linker design or post-synthetic modification, (2) introducing surface corrugation on MOF, and (3) the preparation of hydrophobic MOF composite.[29–31] These strategies aim to minimize the surface free energy of MOFs (weakened attraction between water and MOF) and promote the surface roughness, collectively boosting the hydrophobicity of MOFs. Attractive as these tactics seem, some negative concerns deserve attention: (1) the preparation of perfluorinated/multi-alkylated linkers is sometime tedious; (2) the reproducibility of post-synthetic modification is not guaranteed, giving rise to varying performance; (3) some MOF composites involve time-consuming multi-step preparation. Setting aside these problems, MOFs have been fabricated with other materials to build a composite that merges photothermal

School of Chemical Engineering and Light Industry, Guangdong University of Technology, Guangzhou, 510006, P. R. China. E-mail: junhe@gdut.edu.cn; laihonchung@gdut.edu.cn

This journal is © The Royal Society of Chemistry 2023

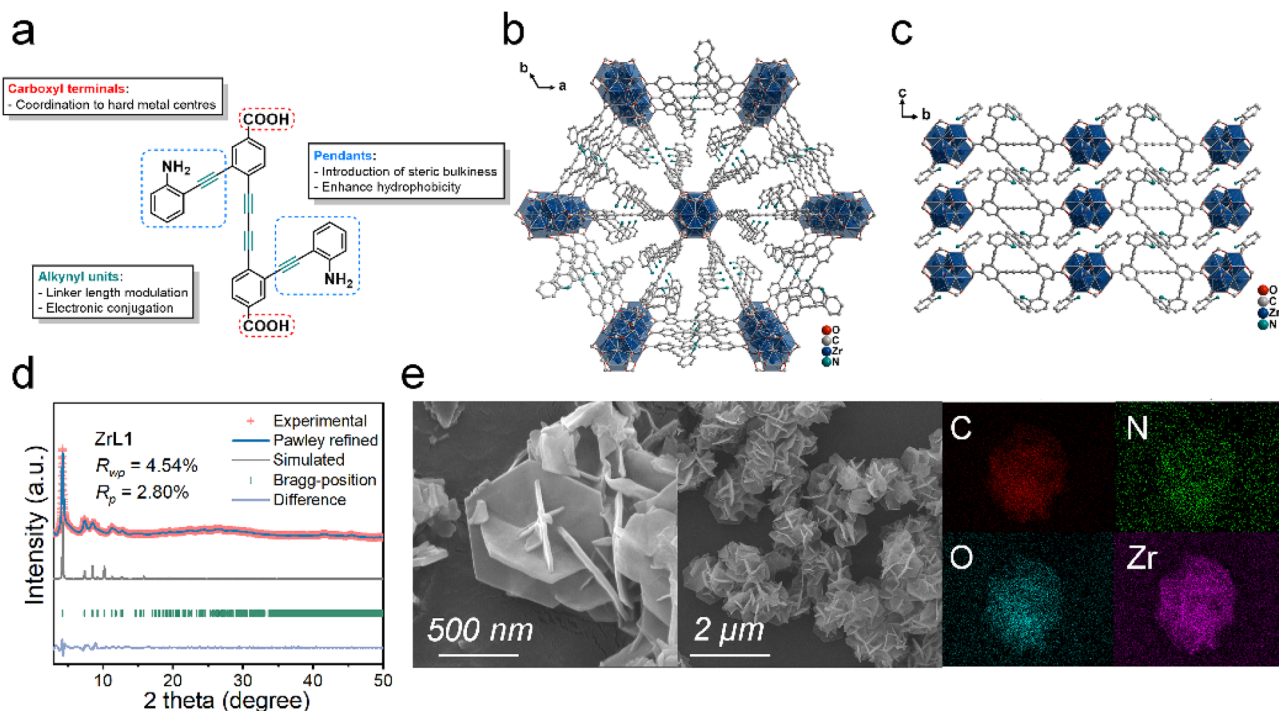*J. Mater. Chem. A*, 2023, **11**, 22223–22231 | **22223**

Fig. 1 (a) Chemical structure of H_2L1; (b) perspective view of hexagonal network of Zr**L1** along the c-axis perpendicular to the ab plane; (c) perspective view of Zr**L1** along the a-axis perpendicular to the bc plane; (d) experimental, Pawley-refined, and simulated XRD patterns of Zr**L1**; (e) SEM images and elemental mapping of Zr**L1**.

conversion and oil/water separation[32–38] for self-cleaning oil/water separation, a more practical execution of water purification and oil extraction.

Considering all these aspects, we designed a backfolded alkyne-rich ditopic linker H_2L1 and aim to construct a two-dimensional (2D) Zr-based MOF possibly with photothermal conversion capacity and hydrophobic–oleophilic nature for photothermally driven oil/water separation supported by the following rationales (Fig. 1a): (1) H_2L1 can be afforded easily by the common homo- and cross-coupling of alkynes; (2) the dicarboxyl main skeleton is used for construction of the framework while the protruding aniline-tethered alkynyl pendants introduce steric hindrance to promote the growth of 2D layered MOF, which is favoured by sterically bulky linkers, as observed in other reported Zr-based 2D MOF;[39] (3) the enrichment of alkynes is for extending the electronic conjugation of the linker to broaden the absorption profiles ready for photothermal conversion as well as connecting more organic moieties to enhance the hydrophobicity/oleophilicity; (4) –NH_2 groups are incorporated to enhance the capture of polar oil by forming dipole interaction. Even though –NH_2 groups in MOF may have better hydrophilicity by forming hydrogen bonds with water,[40–42] –NH_2 at the *ortho*-position is hindered by hydrophobic pendants and main skeleton from strong interaction with water; (5) the adoption of a 2D layered structure is to expose more surface of MOF to oil absorption and for facile dispersal during the fabrication of the composite; (6) Zr^{4+} as a hard acid with high charge density is well-known for binding with hard carboxylate firmly, and the resultant framework is expected to

be stable under various conditions. Gratifyingly, we herein report the preparation of a hydrophobic/superoleophilic 2D Zr-based MOF, namely Zr**L1**. Assembled from H_2L1 and the subsequent fabrication of the composite Zr**L1**@PU (PU = polyurethane) by simple dip-coating. Zr**L1**@PU exhibited decent oil/water separation performance in terms of separation capacity, efficiency, selectivity, and permeability together with excellent mechanical and chemical stability throughout the processes. In addition, Zr**L1**@PU was found photothermally active with good operational stability and capable of evaporating the collected oil by photothermal conversion. It serves as an insightful preliminary study exploring state-of-the-art framework materials for efficient self-cleaning oil/water separator.

Results and discussion

Synthesis and structure characterization of framework

Aniline-functionalised backfolded carboxylic acid terminated linker H_2L1 was prepared by subsequent coupling reactions and hydrolysis (for details, see experimental section in ESI). Heating $ZrCl_4$ and H_2L1 solvothermally in N,N-dimethylformamide (DMF) with HCOOH as a modulator at 90 °C for 48 hours gave Zr**L1** as yellow crystalline solids. Firstly, looking into the Fourier-transform infrared (FT-IR) spectra of H_2L1 and Zr**L1** (Fig. S12†), H_2L1 features amino N–H, alkynyl C≡C, and carboxylic acid C=O stretching signals at about 3457, 2204, and 1650 cm^{-1}; while considering Zr**L1** (whether as-made or activated), both N–H and C≡C stretching signals of H_2L1 still exist

22224 | *J. Mater. Chem. A*, 2023, **11**, 22223–22231

This journal is © The Royal Society of Chemistry 2023

but weaken probably because of the interference by guest species, whereas significant red-shifting of C=O stretching (from 1650 to 1584 cm^{-1}) was found, indicative of the coordination bond between Zr and –COO$^-$. To probe the chemical environment of the elements in Zr**L1**, X-ray photoelectron spectroscopy (XPS) was employed to further identify the status of the elements in the framework. As illustrated in Fig. S18,† Zr, O, C, and N are present in the sample. The Zr 3d XPS spectrum shows two bands at 185.4 and 182.7 eV corresponding to the 3d$_{5/2}$ and 3d$_{3/2}$ signals of the Zr(IV) species. On one hand, the N 1s XPS peak at 400.3 eV comes from the C–N bond, indicating the retention of aniline groups. Moreover, the O 1s XPS spectrum give signals of binding energy at 531.8, 532.8, and 530.7 eV, originating from the C–O, C=O, and Zr–O bonds, respectively, supporting the presence of classical Zr-oxo clusters ligated by carboxylate linkers found in common Zr-based MOF systems.[43]

Even though the as-prepared Zr**L1** is crystalline in nature, a single crystal structure could not be obtained despite numerous attempts. The powder X-ray diffraction (PXRD) measurement of Zr**L1** just gave a pattern showing the sharpest signal at $2\theta = 4.3°$ accompanied by several weaker peaks at $2\theta = 7.4, 8.5, 8.8,$ and $11.3°$ (Fig. 1d) without further insight into the structure. Hence, elemental analysis, thermogravimetric analysis (TGA), and NMR spectroscopy were employed to work out the chemical composition of Zr**L1**. The TG curve of Zr**L1** under air (Fig. S14b†) shows weight loss less than 20% (with weight loss of 6.8% until 100 °C attributed to 11 H_2O molecules) until 360 °C (signifying thermal stability of framework until this point), followed by a steep weight loss beyond 360 °C, resulting in a residual weight of 36.9% (residue left behind as ZrO_2). Besides, the ^{1}H NMR spectrum obtained from digesting Zr**L1** in DMSO-d_6 (with 1 drop HF) at 60 °C for 12 hours (Fig. S13†) reveals that the signals corresponding to H_2**L1** (*i.e.*, consistent number of peaks and splitting pattern; shift in ppm stemming from the addition of HF during digestion), indicating the integrity of the linker in Zr**L1**. Noteworthily, the signal at 8.12 ppm likely refers to HCOOH (Fig. S13a†), around 3.5 to 4 times that of digested **L1**$^{2-}$, probably from the ligated HCOO$^-$ on the Zr–O nodes or guest HCOOH in Zr**L1**. Elemental analysis found that the C (44.65%), H (3.17%), and N (2.78%) for the activated sample of Zr**L1** is fitted with the chemical formula $Zr_6O_4(OH)_4(HCOO)_7(\mathbf{L1})_{2.5}(H_2O)_{11}$ (M_w: 2488.97), which gives a calculated profile of C (44.40%), H (3.16%), and N (2.81%), closely matching the experimental finding.

Given that the $[Zr_6O_8]$ cluster is the connecting node, each node is ideally 12-connected. In stark contrast, Zr**L1** has a significant defect of 58.3% (7/12 × 100%) with each $[Zr_6O_4(OH)_4]$ node bonding to 5 ditopic **L1**$^{2-}$ only. With such heavy defects, it is highly possible that Zr**L1** adopts a 2D structure[44,45] with coordination bond between linkers and $[Zr_6O_4(OH)_4]$ nodes forming on a certain plane to attain a stable structure. Scanning electron microscopy (SEM) conveys an important message that Zr**L1** exists as regular hexagonal plates cluster (Fig. 1e), and it serves as a key clue for structure identification. Based on the 2D morphology and ditopic linker, Zr**L1** most likely features a **hxl** topology (2,6-c network built from 2-c linker and 6-c $[Zr_6O_4(OH)_4]$ node).[46,47] Therefore, the structural

model of Zr**L1** adopting $[Zr_6O_4(OH)_4]$ as the secondary building unit (SBU) and **hxl** net was built based on some MOFs with **hxl** topology.[48–51] The simulated structure of Zr**L1** finally takes up a $P\bar{3}$ space group (no. 147) and honeycomb network, where the central $[Zr_6O_4(OH)_4]$ node links to 6 nodes as vertices to create hexagonal units with each node connecting to 6 **L1**$^{2-}$ along the *ab* plane to produce a layered structure while layers stack along the *c*-axis (Fig. 1b and c).

The PXRD pattern of the simulated structure (trigonal lattice, $a = b = 23.938$ Å, $c = 9.537$ Å, $\alpha = \beta = 90°$, $\gamma = 120°$; Fig. 1d; details of refinement are included in the ESI) matches well with the experimental PXRD pattern of Zr**L1** together with satisfactory agreement factor ($R_{WP} = 4.54\%$ and $R_P = 2.80\%$) from Pawley refinement against experimental PXRD pattern, signifying the correctness of the model. One should know that the model based on **hxl** net is an ideal case in which each $[Zr_6O_4(OH)_4]$ node is 6-connected to **L1**$^{2-}$ while Zr**L1** actually has only 5 **L1**$^{2-}$ on the node, meaning that the steric hindrance by **L1**$^{2-}$ is larger than expected and leads to more defects. However, the high consistency between the simulated and experimental PXRD patterns reveals that the hexagonal network can be kept along with defects distributed evenly over the network, maintaining the network integrity. It is noteworthy that interlayer $[Zr_6O_4(OH)_4]$ nodes possibly merge to give a Zr_{12} cluster, as observed in previously reported metal–organic layer.[52] Such transformation in Zr**L1** may be disfavoured by the sterically bulky linkers in which aniline-tethered alkynyl pendants between each layer are too crowded to allow the forging of $[Zr_6O_4(OH)_4]$ nodes.

From the simulated model, Zr**L1** bears well-defined triangular cavity with a pore width of 18.76 Å, and one would expect it to show some sorption capability. Unexpectedly, Zr**L1** gives low N_2 and CO_2 sorption Brunauer–Emmett–Teller (BET) surface area of 27.065 and 22.908 m^2 g^{-1}, respectively (Fig. S15 and S16†). There are two plausible reasons: (1) the aniline-alkynyl pendants are not merely sterically bulky but also rotating along the alkynyl axis to occupy the space fluxionally; (2) the layered structures stack intimately, further lowering the spatial availability. To evaluate the possibility of Zr**L1** for photothermal application, the optical absorption profile and chemical stability of Zr**L1** were also investigated. UV-visible diffuse reflectance spectroscopy (UV-vis DRS) was employed to measure the absorption profile of Zr**L1**, and the spectrum shows that Zr**L1** features a sharp absorption band centred at 390 nm with tailing until around 700 nm (Fig. S24a†). After Kubelka–Munk transformation, the optical band gap of Zr**L1** was calculated to be 2.69 eV (Fig. S24b†). Afterwards comes the stability test, where Zr**L1** was found to be stable in most of the common organic solvents and aqueous media of extreme pH (pH = 1 or 13); specifically, the PXRD patterns and FT-IR profiles of Zr**L1** are unchanged even after immersing Zr**L1** in different organic solvents and aqueous solution of pH = 1, 3, 10, and 13 (Fig. S20†).

Oil/water separation study

The backfolded alkyne-rich linker designed in this work is specifically for enhancing the hydrophobicity and oleophilicity

This journal is © The Royal Society of Chemistry 2023

J. Mater. Chem. A, 2023, **11**, 22223–22231 | **22225**

of the framework to meet the needs in oil/water separation. The contact angle is a good indicator of sample wettability and hence these two parameters. ZrL1 powder shows the largest water contact angle of 154°, exceeding the superhydrophobicity threshold of 150°. In sharp contrast, the oil droplet flattened rapidly on ZrL1 (*e.g.*, contact angles of dichloromethane, DCM, become 0° within 1.4 seconds, Fig. S21†). These findings suggest that ZrL1 is at the same time hydrophobic and superoleophilic. Considering scenarios beyond neutral water, the contact angles of saline water (3.5 wt% NaCl, pH = 7), acidic solution (0.01 M HCl, pH = 2) and alkaline solution (0.01 M NaOH, pH = 12) on ZrL1 have been measured and found to be 154, 148, and 142° (Fig. S21†), consolidating excellent hydrophobicity of ZrL1. It was found that pristine PU has contact angles of 112° and 0° with respect to water (averagely hydrophobic) and DCM (superoleophilic), implying its shortcomings in oil/water separation. To modify ZrL1 for oil/water separation (*i.e.*, make it a compressible sponge for cycling operation), ZrL1 (10, 20, or 30 mg) was loaded into polyurethane (PU) sponge through simple dip-coating (Fig. 2a), in which the PU sponge was immersed in an ethanolic solution containing well-dispersed ZrL1, followed by the complete evaporation of ethanol. Compared with pristine PU sponge by SEM, the surface of PU sponge roughened after forming the composite with ZrL1 as ZrL1@PU, indicative of the successful introduction of ZrL1 into PU sponge (Fig. 2c, d and S27†). Importantly, the PXRD pattern of ZrL1 was retained apparently in ZrL1@PU in spite of band broadening at high 2θ region (stemming from PU, as

illustrated by its PXRD pattern, Fig. 2b), revealing the framework integrity of ZrL1 and partial amorphization probably due to the random distribution of ZrL1 on the PU surface. Intriguingly, the PXRD pattern of ZrL1@PU is consistent with the original one even after six-month storage (Fig. 2b), highlighting its outstanding stability and lifespan. The loading efficiency can be calculated by the following equation (eqn (1)).

$$\text{loading content}(\%) = \frac{w_1 - w_0}{w_0} \times 100\% \tag{1}$$

where w_0 and w_1 represent the weight before and after dip-coating, respectively, with each sample repeated three times. The loading content (wt%) of ZrL1 reached 20.6, 31.1, and 48.0% for loading amounts of 10.0, 20.0, and 30.0 mg, respectively. The adhesion test was conducted on ZrL1@PU to evaluate its possibility as oil/water separator. When the oil droplet (ethyl acetate, EA) touches ZrL1@PU, it spreads over the surface quickly (Fig. S25a†), highlighting the strong oleophilicity of ZrL1@PU and robust adhesivity of oil on ZrL1@PU. In stark contrast, the water droplet could be repeatedly compressed to/detached from the surface of ZrL1@PU without leaving any adhesion (Fig. S25b†), signifying that the composite inherits the hydrophobicity of ZrL1 and elasticity of PU sponge, which serve as prerequisites for application in oil/water separation. Expectedly, ZrL1@PU shows large contact angles of 147°, 141°, and 145° with respect to salt water (3.5 wt% NaCl, pH = 7), acidic solution (0.01 M HCl, pH = 2), and alkaline solution (0.01 M NaOH, pH = 12) (Fig. S26†), just like ZrL1.
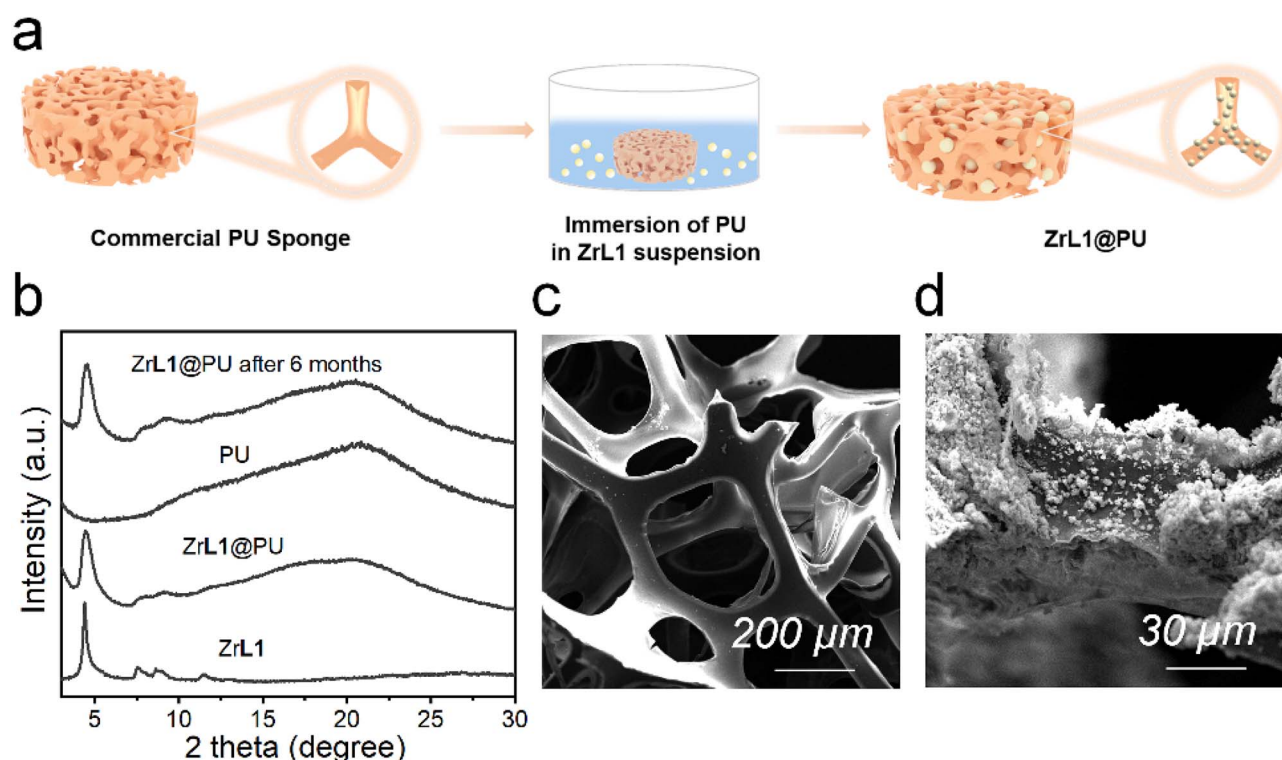

Fig. 2 (a) Schematic depiction of preparation of ZrL1@PU; (b) PXRD patterns (Cu Kα, λ = 1.5418 Å) of ZrL1 and as made ZrL1@PU, PU, and ZrL1@PU stored for six months; SEM images of (c) PU sponge and (d) ZrL1@PU.

22226 | *J. Mater. Chem. A*, 2023, **11**, 22223–22231

This journal is © The Royal Society of Chemistry 2023

To further study the hydrophilicity and oleophilicity of Zr**L1** and Zr**L1**@PU, Zr**L1** was added to pure water and DCM, respectively, as a demonstration. As revealed in Fig. S29c,† Zr**L1** powders float on water surface while they sink to the bottom of the organic phase, revealing the hydrophobic nature of Zr**L1**. Noteworthily, naked PU sank down to the bottom of water whereas Zr**L1**@PU kept floating on the water surface (Fig. S29a†). Incredibly, even though Zr**L1**@PU was pressed in water, it immediately got back to the water surface after being released. These again highlight the combination of elasticity of PU and hydrophobic nature of Zr**L1** in Zr**L1**@PU. It is worth noting that silver mirror phenomenon observed for Zr**L1**@PU under water comes from an even air layer established between the water phase and hydrophobic surface of Zr**L1**@PU (Fig. S29b†), consolidating the hydrophobicity of Zr**L1**@PU.

To evaluate the absorption selectivity, Zr**L1**@PU was used to remove EA floating on water surface and DCM at the bottom of water (both organic species dyed by methyl red) (Fig. S29d and e†) as illustrative examples. When a piece of Zr**L1**@PU was taken to contact EA or DCM, the polluted area vanished within seconds and left behind was transparent water. The absorbed dyed solvent could be extracted from Zr**L1**@PU thoroughly by simply squeezing the sponge. To investigate in a quantitative way, the absorption capacity of Zr**L1**@PU (10 mg of Zr**L1** loaded) towards EA, toluene, DCM, acetone, chloroform, and tetrachloromethane was tested (Fig. 3b) and calculated by the following equation (eqn (2)).

$$\text{absorption capacity}\left(\text{g g}^{-1}\right) = \frac{w_a - w_i}{w_i} \tag{2}$$

where w_a and w_i represent weights of sample after and before absorption respectively, with the final capacity calculated from averaging three runs. As shown in Fig. 3b and S28,† the absorption capacity of Zr**L1**@PU for chloroform reached 66.19 g g^{-1} while it was still 43.43 g g^{-1} for acetone (lowest density among the tested samples; for absorption capacity towards the rest of the oils, see Table S2†). The absorption capacity of selected oil species by Zr**L1**@PU is comparable to the top level and better than most other MOF-based absorbents[53–66] (Table S3†). As the recyclability and operational stability of the absorbent are of paramount importance in industrial prospects, Zr**L1**@PU was taken for 20 absorption/desorption cycles. Taking chloroform, DCM, and EA as examples, Zr**L1**@PU maintained constant absorption capacity throughout 20 cycles (Fig. 3c and S28†), highlighting the superb solvent tolerance, absorption/desorption stability, and recyclability of Zr**L1**@PU.

To study the oil/water separation efficiency, a separation setup depicted in Fig. S31† was built. Zr**L1**@PU was settled horizontally as a membrane of the column outlet, followed by the addition of the analyte (organic phase and aqueous phase, 1 : 1, v/v) and subsequently by elution under gravitational pull. As seen in Fig. S31,† the organic phase (DCM dyed by methyl red) got through Zr**L1**@PU while the aqueous phase (dyed by methylene blue) was blocked by Zr**L1**@PU. Also, no aqueous phase was found in the measuring cylinder for collecting the eluted organic phase. It works out for light oil (EA)/water
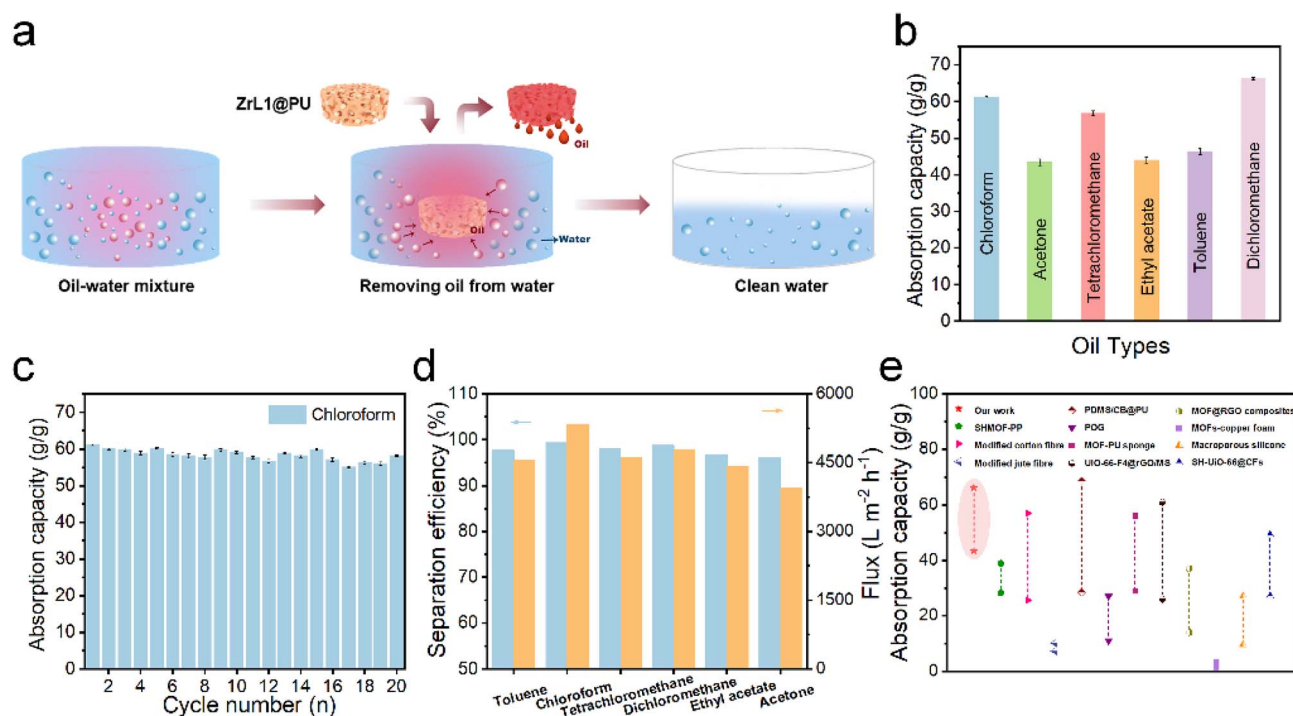

Fig. 3 (a) Schematic illustration of oil removal from water through absorption by Zr**L1**@PU; (b) organic solvent absorption capacities of Zr**L1**@PU (the errors are estimated to vary from ±1.4% to ±3.2%); (c) absorption capacity of Zr**L1**@PU for chloroform throughout 20 cycles of absorption; (d) separation efficiency and flux of oils studied in this work in oil/water separation by Zr**L1**@PU; (e) comparison of absorption capacities of selected absorbents with Zr**L1**@PU.

This journal is © The Royal Society of Chemistry 2023

J. Mater. Chem. A, 2023, **11**, 22223–22231 | **22227**

separation (Fig. S32†). These findings suggest that ZrL1@PU separates oil from the aqueous solution by blocking water. To have quantitative comparison, pure PU and ZrL1@PU loaded with 10.0, 20.0, and 30.0 mg ZrL1 were taken for DCM/water separation. The separation efficiency is obtained as follows (eqn (3)).

$$\text{separation efficiency}(\%) = \frac{V_p + V_s}{V_o} \times 100\% \qquad (3)$$

where V_o denotes the volume of oil in the original oil/water mixture, V_p refers to the volume of oil collected by the measuring cylinder, and V_s represents the volume of residual oil collected by squeezing ZrL1@PU after the separation run. The results showed that ZrL1@PU with different loaded amounts of ZrL1 give similar separation efficiency of *ca.* 98%, revealing that the least loading amount (10 mg) of ZrL1 is enough for constructing ZrL1@PU to execute efficient oil/water separation and outperform primitive PU (Fig. S30a†). As a whole, ZrL1@PU was tested the oil/water separation efficiency with toluene, DCM, chloroform, tetrachloromethane, EA, and petroleum ether (PE) as organic phases. Enchantingly, the separation efficiency for chloroform/water mixture was the highest at 99.3% and the lowest for PE/water mixture still reached 96.2% (Fig. 3d, for the separation efficiency of other oils in this study, see Table S2†), presenting the generality of ZrL1@PU as a separator for oil/water emulsion. Differentiation in separation efficiency may originate from the divergence of water solubility and volatility in various oils. Furthermore, the oil permeability of ZrL1@PU with respect to all the studied oil/water mixture was investigated and worked out by the following equation (eqn (4)).

$$\text{oil permeability}(\text{flux}) = \frac{\Delta V}{A \times T} \qquad (4)$$

where ΔV denotes the volume of oil passing through ZrL1@PU, A refers to the effective separation area, T represents the permeation time; final oil permeability comes from average results of three runs. The trend of flux density follows that of separation efficiency with chloroform (5340 L m^{-2} h^{-1}) and PE (3956 L m^{-2} h^{-1}) to be highest and lowest, respectively (Fig. 3d, for the flux density of other oils in this study, see Table S2†). Low density of the oil may account for lower flux for oil/water separation. It should be noted that low-density oil takes longer to get through denser aqueous phase to pass through the separating material, resulting in lower collection amount. To further evaluate the recyclability and applicability, ZrL1@PU was used to separate DCM/water and DCM/saline water (3.5 wt% NaCl, mimicking oceanic oil spillage) mixtures. The separation efficiency of ZrL1@PU remained almost steady above 96.4% in both water or saline water mixture even for 9 separation cycles (Fig. S30b†), again indicating the extraordinary recyclability and operational stability of ZrL1@PU as the oil/water separator.

Photothermal conversion and solar-assisted evaporation

Since ZrL1 exhibits absorption covering almost the full UV-visible spectral region and excellent chemical tolerance in various solution media, this framework material is of great potential to harvest light for photothermal application in various scenarios. Under one-sun irradiation (420–2500 nm) simulated with a xenon lamp (1.0 kW m^{-2}), the ZrL1 powders (10.0, 20.0 or 30.0 mg) also exhibited solar-thermal conversion. To be specific, after eight minutes, 30.0 mg ZrL1 could reach a maximum temperature of 57.6 °C while 20.0 and 10.0 mg of ZrL1 only attained 54.2 and 51.2 °C, respectively (Fig. S33b†). Because of the decent performance shown by 10.0 mg ZrL1, ZrL1 at this amount was taken for photothermal conversion under different powers of irradiation and cycling stability test. Upon irradiation at different powers (1.0, 2.0, 3.0, and 5.0 kW m^{-2}) for eight minutes, ZrL1 (10.0 mg) could reach the maximum temperature as high as 122.5 °C at the highest irradiation power used (5.0 kW m^{-2}) (Fig. S33d†). Also, ZrL1 was found to be resistant to photobleaching, as reflected by the consistent maximum temperatures throughout five cycles of xenon-lamp on–off irradiation (Fig. S33c†). Likewise, ZrL1@PU composites exhibit satisfactory photothermal performance. By xenon lamp irradiation (1.0 kW m^{-2}, 420–2500 nm, simulated one-sun light) for eight minutes, ZrL1@PU gave the highest maximum temperatures of 89.4 °C for the composite loaded with 30.0 mg ZrL1 and even around 83.0 and 87.5 °C for the composite loaded with 10.0 and 20.0 mg of ZrL1, respectively, outweighing photothermally inactive pure PU (34.8 °C) (Fig. 4b). Since the divergence in maximum temperatures achieved using 30.0 mg or 10.0 mg is not significant, the composite involving as least ZrL1 as possible is more competent and competitive for further photothermal application. Therefore, ZrL1@PU loaded with 10.0 mg ZrL1 was adopted for all the following investigations unless otherwise stated. More importantly, ZrL1@PU reached maximum temperature of 82.8 °C constantly throughout five cycles of xenon-lamp on–off irradiation (1.0 kW m^{-2}, 420–2500 nm, simulated one-sun light, Fig. 4c), followed by rapid cooling to room temperature within 30 seconds after the removal of irradiation (Fig. 4b), highlighting its efficient photoresponsivity. Like ZrL1, the photothermal performance of ZrL1@PU is better along with the higher power densities of xenon lamp applied (increasing maximum temperature from 1.0 to 5.0 kW m^{-2} and reached the highest of 160.5 °C at a power density of 5.0 kW m^{-2}, Fig. 4d). Enlighteningly, ZrL1@PU is operationally stable throughout the repeated photothermal experimentation, as demonstrated by the consistent PXRD patterns and FT-IR profiles of ZrL1 before and after repeated cycles of photothermal conversion (Fig. S36,† ZrL1 collected from ZrL1@PU by ultrasonication after five photothermal cycles for measurement).

Based on the outstanding oil/water separation capacity/efficiency and photothermal conversion performance, ZrL1@PU can be applied as a photothermal oil/water separator in which the oil absorbed by ZrL1@PU can be released and collected by photothermally driven evaporation. Using DCM and EA for demonstration, without illumination, the evaporation rates of DCM and EA in both pristine PU and ZrL1@PU were similar (Fig. 4e and S35†). Upon xenon lamp irradiation (1.0 kW m^{-2}, 420–2500 nm, simulated one-sun light), the evaporation rates of both DCM and EA in ZrL1@PU are apparently faster than that in PU. Specifically, DCM and EA in
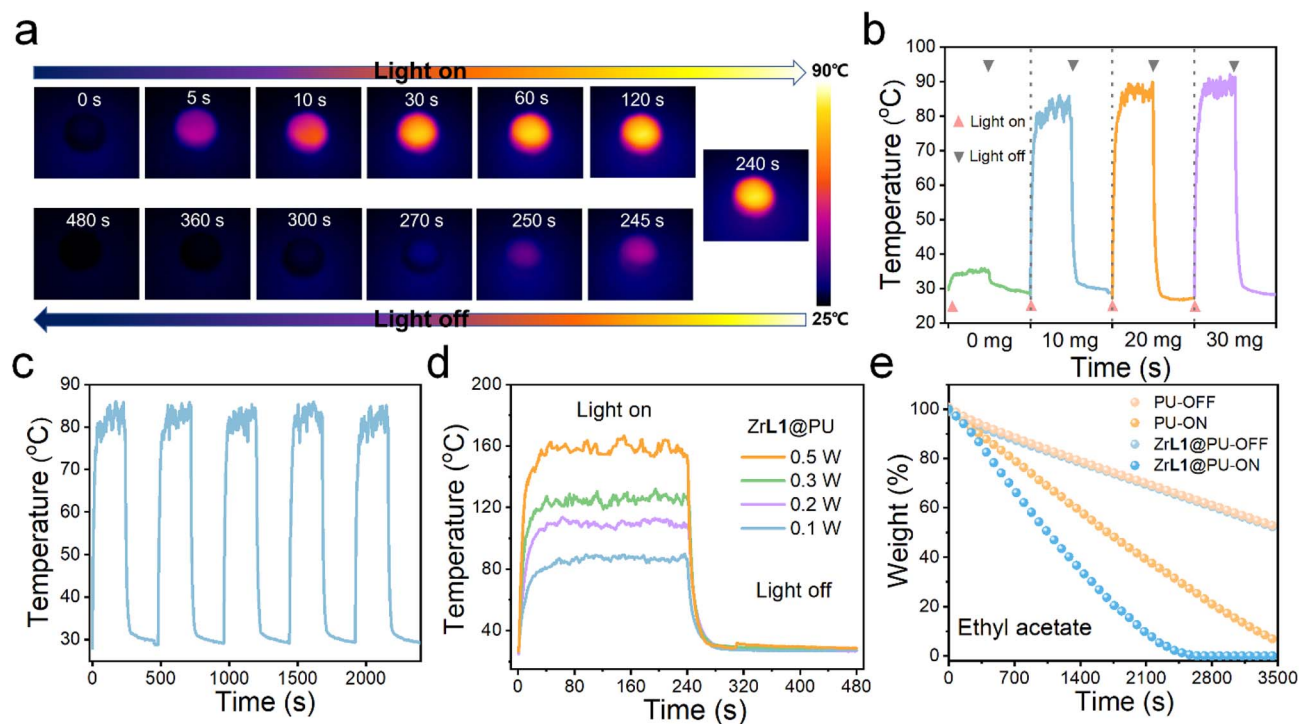
Fig. 4 (a) IR thermal images of ZrL1@PU under xenon lamp (1.0 kW m^{-2}); (b) photothermal conversion behaviour of PU and ZrL1@PU under one-sun irradiation within eight minutes; (c) anti-photobleaching property of ZrL1@PU during five cycles of heating–cooling; (d) photothermal conversion behaviour of ZrL1@PU under different light intensities (1.0, 2.0, 3.0, and 5.0 kW m^{-2}); (e) photo-driven distillation of ZrL1@PU. Weight variations of PU or ZrL1@PU saturated by EA with/without light illumination at a power density of 1.0 kW m^{-2}.

ZrL1@PU could be completely evaporated within 25 and 40 minutes, respectively, but those in PU remained over 30% for the same illumination period (Fig. 4e and S35†). To our delight, the PXRD patterns and FT-IR profiles of ZrL1 from ZrL1@PU after 20 cycles of solvent evaporation (ZrL1 recovered from ZrL1@PU by ultrasonication after 20 evaporation cycles for measurement) are consistent with those collected from the original ZrL1 (Fig. S36†) underlying its structural integrity throughout the repeated operation of solvent evaporation. ZrL1@PU represents a prototype of photothermally-driven self-cleaning oil/water separator to be applied at the oil spillage site.

Conclusions

A state-of-the-art designed backfolded aniline-tethered alkyne-rich ditopic carboxylate linker was successfully assembled with [Zr$_6$O$_4$(OH)$_4$] nodes to generate a 2D hexagonally packed network, ZrL1. Gifted with hydrophobicity and super-oleophilicity, ZrL1 was fabricated with PU sponge to be a composite material exhibiting excellent capacity (as high as 66.19 g g^{-1} of DCM), efficiency (as high as 99.3%), selectivity (no take up of aqueous portion), and permeability (as high as 5340 L m^{-2} h^{-1} of DCM) in oil/water separation. Also, benefiting from extended alkynyl bridges, ZrL1 features absorption covering almost the whole UV-visible spectral region and hence was found to be active for photothermal conversion. As a result, ZrL1@PU was studied preliminarily as a prototype of self-cleaning photothermally driven oil/water separator showing

decent solvent evaporation rate and robust recyclability as well as outstanding durability. The demonstration in this work undoubtedly offers opportunities into the design of hydrophobic/oleophilic structurally well-defined, robust framework for self-cleaning photothermally driven oil/water separation.

Author contributions

Conflicts of interest

There are no conflicts of interest to declare.

Acknowledgements

This journal is © The Royal Society of Chemistry 2023

J. Mater. Chem. A, 2023, 11, 22223–22231 | 22229

References

1 S. E. Chang, *Nat. Sustain.*, 2021, **4**, 1023–1024.

2 M. Kamali, M. E. Costa, T. M. Aminabhavi and I. Capela, *Chem. Eng. J.*, 2019, **370**, 1511–1521.

3 R. K. Gupta, G. J. Dunderdale, M. W. England and A. Hozumi, *J. Mater. Chem. A*, 2017, **5**, 16025–16058.

4 Y. Guan, F. Cheng and Z. Pan, *Polymers*, 2019, **11**, 806.

5 X. Yan, X. Xiao, C. Au, S. Mathur, L. Huang, Y. Wang, Z. Zhang, Z. Zhu, M. J. Kipper, J. Tang and J. Chen, *J. Mater. Chem. A*, 2021, **9**, 21659–21684.

6 U. Baig, M. Faizan and A. Waheed, *Adv. Colloid Interface Sci.*, 2022, **303**, 102635.

7 B. Xiang, Q. Liu, Q. Sun, J. Gong, P. Mu and J. Li, *Chem. Commun.*, 2022, **58**, 13413–13438.

8 E. S. Dmitrieva, T. S. Anokhina, E. G. Novitsky, V. V. Volkov, I. L. Borisov and A. V. Volkov, *Polymers*, 2022, **14**, 980.

9 Q. Fan, T. Lu, Y. Deng, Y. Zhang, W. Ma, R. Xiong and C. Huang, *Sep. Purif. Technol.*, 2022, **297**, 121445.

10 Y. Yang, Z. Guo and W. Lu, *Small*, 2022, **18**, 2204624.

11 B. Li, B. Qi, Z. Guo, D. Wang and T. Jiao, *Chemosphere*, 2023, **327**, 138528.

12 M. Gu, Y. Qin, X. Wang, S. Li, Y. Sun, M. Xue, J. Ji and X. Zang, *Ind. Eng. Chem. Res.*, 2023, **62**, 11757–11767.

13 M. Awwad, M. Bilal, M. Sajid, M. S. Nawaz and I. Ihsanullah, *J. Environ. Chem. Eng.*, 2023, **11**, 109073.

14 W. Zhang, Y. Liu, F. Tao, Y. An, Y. Zhong, Z. Liu, Z. Hu, X. Zhang and X. Wang, *Sep. Purif. Technol.*, 2023, **316**, 123767.

15 H. Saini, E. Otyepková, A. Schneemann, R. Zbořil, M. Otyepka, R. A. Fisher and K. Jayaramulu, *J. Mater. Chem. A*, 2022, **10**, 2751–2785.

16 C. Wang, D. Liu and W. Lin, *J. Am. Chem. Soc.*, 2013, **135**, 13222–13234.

17 Y.-S. Wei, M. Zhang, R. Zou and Q. Xu, *Chem. Rev.*, 2020, **120**, 12089–12174.

18 V. Pascanu, G. González Miera, A. K. Inge and B. Martín-Matute, *J. Am. Chem. Soc.*, 2019, **141**, 7223–7234.

19 J. Canivet, A. Fateeva, Y. Guo, B. Coasne and D. Farrusseng, *Chem. Soc. Rev.*, 2014, **43**, 5594–5617.

20 N.-X. Zhu, Z.-W. Wei, C.-X. Chen, D. Wang, C.-C. Cao, Q.-F. Qiu, J. J. Jiang, H.-P. Wang and C.-Y. Su, *Angew. Chem., Int. Ed.*, 2019, **58**, 17033–17040.

21 F. Luo, X. Liang, W. Chen, S. Wang, X. Gao, Z. Zhang and Y. Fang, *Chem. Eng. J.*, 2023, **465**, 142891.

22 J. Zheng, R. S. Vemuri, L. Estevez, P. K. Koech, T. Varga, D. M. Camaioni, T. A. Blake, B. P. McGrail and R. K. Motkuri, *J. Am. Chem. Soc.*, 2017, **139**, 10601–10604.

23 Y. Song, J. Phipps, C. Zhu and S. Ma, *Angew. Chem., Int. Ed.*, 2023, **62**, e202216724.

24 Y. Xie, Z. Liu, Y. Gang, H. Li, N. Wang, Y. Song, X. Wang, J. Chen, J. Wang, S. Ma and G. Ye, *Chem. Soc. Rev.*, 2023, **52**, 97–162.

25 Q.-G. Zhai, X. Bu, X. Zhao, D.-S. Li and P. Feng, *Acc. Chem. Res.*, 2017, **50**, 407–417.

26 E. Binaeian, E. M. El-Sayed, M. K. Matikolaei and D. Yuan, *Coord. Chem. Rev.*, 2021, **430**, 213738.

27 D.-X. Liu, Z.-H. Yu, X.-X. Chen, W.-X. Zhang and X.-M. Chen, *Chin. Chem. Lett.*, 2023, **34**, 107310.

28 S.-N. Sun, L.-Z. Dong, J.-R. Li, J.-W. Shi, J. Liu, Y.-R. Wang, Q. Huang and Y.-Q. Lan, *Angew. Chem., Int. Ed.*, 2022, **61**, e202207282.

29 K. Jayaramulu, F. Geyer, A. Schneemann, Š. Kment, M. Otyepka, R. Zbořil, D. Vollmer and R. A. Fischer, *Adv. Mater.*, 2019, **31**, 1900820.

30 M. Zhang, X. Xin, Z. Xiao, R. Wang, L. Zhang L and D. Sun, *J. Mater. Chem. A*, 2017, **5**, 1168–1175.

31 S. Mukherjee, A. M. Kansara, D. Saha, R. Gonnade, D. Mullangi, B. Manna, A. V. Desai, S. H. Thorat, P. S. Singh, A. Mukherjee and S. K. Ghosh, *Chem.–Eur. J.*, 2016, **22**, 10937–10943.

32 J. Cao, Y. Su, Y. Liu, J. Guan, M. He, R. Zhang and Z. Jiang, *J. Membr. Sci.*, 2018, **566**, 268–277.

33 W. Li, P. Xu, Z. Wang, Y. He, H. Qin, Y. Zeng, Y. Li, Z. Zhang and J. Gao, *Mater. Chem. Front.*, 2023, DOI: [10.1039/D3QM00487B](10.1039/D3QM00487B).

34 Y. Hu, Y. Jiang, L. Ni, Z. Huang, L. Liu, Q. Ke and H. Xu, *J. Hazard. Mater.*, 2023, **443**, 130339.

35 G. Chen, Z. Jiang, A. Li, X. Chen, Z. Ma and H. Song, *J. Mater. Chem. A*, 2021, **9**, 16805–16813.

36 A. Raj, R. M. Rego, K. V. Ajeya, H.-Y. Jung, T. Altalhi, G. M. Neelgund, M. Kigga and M. D. Kurkuri, *Chem. Eng. J.*, 2023, **453**, 139757.

37 A. Mähringer, M. Hennemann, T. Clark, T. Bein and D. D. Medina, *Angew. Chem., Int. Ed.*, 2021, **60**, 5519–5526.

38 L. Feng, S.-H. Lo, K. Tan, B.-H. Li, S. Yuan, Y.-F. Lin, C.-H. Lin, S.-L. Wang, K.-L. Lu and H.-C. Zhou, *Matter*, 2020, **2**, 988–999.

39 G. Lan, Y. Quan, M. Wang, G. T. Nash, E. You, Y. Song, S. S. Veroneau, X. Jiang and W. Lin, *J. Am. Chem. Soc.*, 2019, **141**, 15767–15772.

40 G. Liu, Y. Cai, H. Yuan, J. Zhang, Z. Zhang and D. Zhao, *J. Membr. Sci.*, 2023, **668**, 121077.

41 R. Wang, M. Wei and Y. Wang, *J. Membr. Sci.*, 2020, **604**, 118090.

42 T. Xu, F. Sheng, B. Wu, M. A. Shehzad, A. Yasmin, X. Wang, Y. He, L. Ge, X. Zheng and T. Xu, *J. Membr. Sci.*, 2020, **615**, 118608.

43 A. K. Kar, R. Sarkar, A. K. Manal, R. Kumar, S. Chakraborty, R. Ahija and R. Srivastava, *Appl. Catal., B*, 2023, **325**, 122385.

44 G. Lan, Z. Li, S. S. Veroneau, Y.-Y. Zhu, Z. Xu, C. Wang and W. Lin, *J. Am. Chem. Soc.*, 2018, **140**, 12369–12373.

45 T. Luo, Y. Fan, J. Mao, E. Yuan, E. You, Z. Xu and W. Lin, *J. Am. Chem. Soc.*, 2022, **144**, 5241–5246.

46 D. Kim, X. Liu and M. S. Lah, *Inorg. Chem. Front.*, 2015, **2**, 336–360.

47 H. Jiang, D. Alezi and M. Eddaoudi, *Nat. Rev. Mater.*, 2021, **6**, 466–487.

48 J. Jia, A. J. Blake, N. R. Champness, P. Hubberstey, C. Wilson and M. Schröder, *Inorg. Chem.*, 2008, **47**, 8652–8664.

22230 | *J. Mater. Chem. A*, 2023, **11**, 22223–22231

This journal is © The Royal Society of Chemistry 2023

49 H. L. Nguyen, F. Gándara, H. Furukawa, T. L. H. Doan, K. E. Cordova and O. M. Yaghi, *J. Am. Chem. Soc.*, 2016, **138**, 4330–4333.

50 V. Sharma, D. De, S. Pal, P. Saha and P. K. Bharadwaj, *Inorg. Chem.*, 2017, **56**, 8847–8855.

51 W. Lin, E. Ning, L. Yang, Y. Rao, S. Peng and Q. Li, *Inorg. Chem.*, 2021, **60**, 11756–11763.

52 P. Ji, K. Manna, Z. Lin, X. Feng, A. Urban, Y. Song and W. Lin, *J. Am. Chem. Soc.*, 2017, **139**, 7004–7011.

53 P. Cherukupally, W. Sun, A. P. Y. Wong, D. R. Williams, G. A. Ozin, A. M. Bilton and C. B. Park, *Nat. Sustain.*, 2020, **3**, 136–143.

54 C. Gogoi, A. Rana, S. Ghosh, R. Fopase, L. M. Pandey and S. Biswas, *ACS Appl. Nano Mater.*, 2022, **5**, 10003–10014.

55 N. Lv, X. Wang, S. Peng, L. Luo and R. Zhou, *RSC Adv.*, 2018, **8**, 30257–30264.

56 N. Lv, X. Wang, S. Peng, H. Zhang and L. Luo, *Int. J. Environ. Res. Public Health*, 2018, **15**, 969.

57 J. Chen, M. Sun, Y. Ni, T. Zhu, J. Haung, X. Li and Y. Lai, *J. Hazard. Mater.*, 2023, **445**, 130541.

58 F. I. Alghunaimi, D. J. Alsaeed, A. M. Harith and T. A. Saleh, *J. Cleaner Prod.*, 2019, **233**, 946–953.

59 Z. He, H. Wu, Z. Shi, X. Duan, S. Ma, J. Chen, Z. Kong, A. Chen, Y. Sun and X. Liu, *Colloids Surf., A*, 2022, **648**, 129142.

60 Y. Zhan, S. He, J. Hu, S. Zhao, G. Zeng, M. Zhou, G. Zhang and A. Sengupta, *J. Hazard. Mater.*, 2020, **388**, 121752.

61 J. Gu, H. Fan, C. Li, J. Caro and H. Meng, *Angew. Chem., Int. Ed.*, 2019, **58**, 5297–5301.

62 J. Du, C. Zhang, H. Pu, Y. Li, S. Jin, L. Tan, C. Zhou and L. Dong, *Colloids Surf., A*, 2019, **573**, 222–229.

63 J. Cao, D. Wang, P. An, J. Zhang and S. Feng, *J. Mater. Chem. A*, 2018, **6**, 18025–18030.

64 X. Wang, Z. Liu, X. Liu, Y. Su, J. Wang, T. Fan, X. Ning, S. Ramakrishn and Y.-Z. Long, *Carbon*, 2022, **193**, 77–87.

65 Y. Zhang, S. Hou, H. Song, G. Qin, P. Li, K. Zhang, T. Li, L. Han, W. Liu and S. Ji, *J. Hazard. Mater.*, 2023, **451**, 131064.

66 R. Dalapati, S. Nandi, C. Gogoi, A. Shome and S. Biswas, *ACS Appl. Mater. Interfaces*, 2021, **13**, 8563–8573.

This journal is © The Royal Society of Chemistry 2023

J. Mater. Chem. A, 2023, **11**, 22223–22231 | **22231**